Production of $\Sigma^{\pm}$ Multibody Final States in 5.5-GeV/c K^-p Interactions*

U. E. KRUSE, J. S. LOOS,† AND E. L. GOLDWASSER‡
Department of Physics, University of Illinois, Urbana, Illinois 61801
(Received 1 July 1968)

Experimental results are presented for the reactions $K^-p \to \Sigma^+\pi^-\pi^0$ (1), $K^-p \to \Sigma^-\pi^+\pi^0$ (2), $K^-p \to \Sigma^{\pm}\pi^{\mp}\pi^+\pi^-$ (3) and (4), $K^-p \to \Sigma^{\pm}\pi^{\mp}K^+K^-$ (5) and (6), and $K^-p \to \Sigma^{\pm}\pi^{\mp}\pi^+\pi^-\pi^0$ (7) and (8). The data were obtained in a hydrogen bubble chamber exposed to 5.5-GeV/c incident K^- mesons. This report is based on the analysis of a K^- track length equivalent to 0.27 μb per event. Cross sections for (1)–(8) are presented. Reaction (1) is used to study the $\Sigma^+\rho^-(770)$ channel, and the results are compared to a Regge-model prediction made by Arnold. Reactions (2)–(8) are used to compile cross sections and production cosine distributions for (Y_0^*+neutral meson) channels. Quasi-three-body production is observed in reactions (3), (4), and (7) for the channels $Y_0^*(1405)\pi^+\pi^-$, $Y_0^*(1520)\pi^+\pi^-$, $\Sigma^{\pm}\pi^{\mp}\rho^0(770)$, and $\Sigma^+\pi^-\omega^0(783)$. The production properties of the quasi-three-body final states suggest the presence of multiperipheral mechanisms. In reactions (7) and (8), a search was made for the $\delta^{\pm}(960)$ meson, with inconclusive results.

I. INTRODUCTION

We report on the following reactions from K^-p interactions at 5.5 GeV/c:

$$K^-p \to \Sigma^+\pi^-\pi^0, \quad (1)$$
$$\to \Sigma^-\pi^+\pi^0, \quad (2)$$
$$\to \Sigma^+\pi^-\pi^+\pi^-, \quad (3)$$
$$\to \Sigma^-\pi^+\pi^+\pi^-, \quad (4)$$
$$\to \Sigma^+\pi^-K^+K^-, \quad (5)$$
$$\to \Sigma^-\pi^+K^+K^-, \quad (6)$$
$$\to \Sigma^+\pi^-\pi^+\pi^-\pi^0, \quad (7)$$
$$\to \Sigma^-\pi^+\pi^+\pi^-\pi^0. \quad (8)$$

Previous experimental work on these reactions at incident K^- momenta above 2.0 GeV/c has been reported at the following momenta (in GeV/c): 2.24,[1] 2.65,[2,3] 3.0,[4] 3.5,[5,6] 4.25,[7] 4.6 and 5.0,[8] and 6.0.[9]

This experiment is essentially exploratory in nature. At 5.5 GeV/c, cross sections for reactions (1)–(8) are of the order of 100 μb; consequently, in most channels the number of observed events is so small that only the gross features can be studied.

A discussion of experimental procedure is given in Sec. II. Experimental results are given in Sec. III, with each final state (1)–(8) discussed in turn. Cross sections for reactions (1)–(8) are given in Sec. III A. The properties of the $\Sigma^+\rho^-(770)$ channel are presented and discussed in Sec. III B. Cross sections and production cosine distributions for (Y_0^*+neutral meson) channels are reported in Secs. III C, III D 6, III E 2, and III F. In Secs. III D 7 and III E 3, we present and discuss the production features of the quasi-three-body final states $Y_0^*\pi^+\pi^-$, $\Sigma^{\pm}\pi^{\mp}\rho^0$, and $\Sigma^+\pi^-\omega^0$. The results of a search for the $\delta^{\pm}(960)$ meson in reactions (7) and (8) are given in Sec. III E 4. A brief summary is provided in Sec. IV.

II. EXPERIMENTAL PROCEDURE

A. Bubble-Chamber Exposure

The data were obtained using the Argonne ZGS separated beam transport system[10] and the MURA 30-in. hydrogen bubble chamber.[11] A brief account of the beam-transport system and the bubble chamber has been given by Schweingruber *et al.*[12] in a report on different final states from the same exposure of film. In this paper we report on the analysis of a K^- track length equivalent to 0.27 μb per event, as determined by a beam track count method and checked by a count of $K^-\tau$ decays.

* Work supported in part by the U. S. Atomic Energy Commission.

† Based in part on a thesis submitted in partial fulfillment of the requirements for the Ph.D. degree at the University of Illinois, Urbana, Illinois. Present address: Stanford Linear Accelerator Center, Stanford, Calif.

‡ Present address: National Accelerator Laboratory, Batavia, Ill.

[1] G. W. London, R. R. Rau, N. P. Samios, S. S. Yamamoto, M. Goldberg, S. Lichtman, M. Primer, and J. Leitner, Phys. Rev. **143**, 1034 (1966).

[2] P. Eberhard, F. T. Shively, R. R. Ross, D. M. Siegel, J. R. Ficenec, R. I. Hulsizer, D. W. Mortara, M. Pripstein, and W. P. Swanson, Phys. Rev. Letters **14**, 466 (1965).

[3] P. Eberhard, M. Pripstein, F. T. Shively, U. E. Kruse, and W. P. Swanson, Phys. Rev. **163**, 1446 (1967).

[4] Paris-Saclay-Amsterdam Collaboration, Rept No. CEA-R3037, Centre d'Etude Nucléaire, Saclay, 1966 (unpublished).

[5] Birmingham-Glasgow-London (I.C.)-Oxford-Rutherford Collaboration, Phys. Rev. **152**, 1148 (1966).

[6] J. G. Loken, Ph.D. thesis, Oxford (unpublished).

[7] M. B. Einschlag, T. B. Day, G. P. Yost, G. B. Yodh, and R. G. Glasser, Bull. Am. Phys. Soc. **13**, 704 (1968).

[8] M. Primer, M. Goldberg, K. Jaeger, V. Barnes, P. Dornan, I. Skillicorn, and Jack Leitner, Phys. Rev. Letters **20**, 610 (1968).

[9] W. W. M. Allison, A. Cruz, W. Schrankel, M. M. Hague, S. K. Tuli, P. J. Finney, C. M. Fisher, J. D. Gordon, R. M. Turnbull, R. Erskine, K. Sisterson, K. Paler, P. Chaudhuri, A. Eskreys, and S. J. Goldsack, Phys. Letters **25B**, 619 (1967).

[10] T. H. Fields, E. L. Goldwasser, and U. E. Kruse, Argonne National Laboratory Report No. THF/ELG/UEK-1, 1961 (unpublished).

[11] J. A. Froelich, Argonne National Laboratory Report No. JAF-1, 1965 (unpublished).

[12] F. Schweingruber, M. Derrick, T. Fields, David Griffiths, L. G. Hyman, R. J. Jabbur, J. Loken, R. Ammar, R. E. P. Davis, W. Kropac, and J. Mott, Phys. Rev. **166**, 1317 (1968).

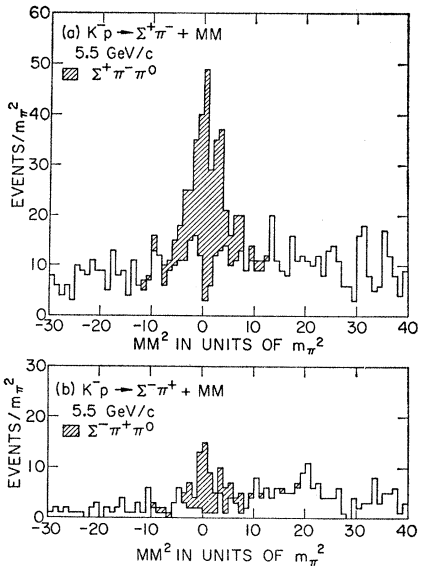

FIG. 1. Distribution of MM^2 for the (two-prong plus kink) events. (a) $K^-p \to \Sigma^+\pi^-$+MM, $\Sigma^+ \to \pi^+n$ or $p\pi^0$; (b) $K^-p \to \Sigma^-\pi^+$+MM, $\Sigma^- \to \pi^-n$. The shaded events are those which have been selected as one-constraint fits with an unseen π^0. Four-constraint events ($K^-p \to \Sigma^\pm\pi^\mp$) have been omitted. For the Σ^+ events, there may be up to four points plotted per event (two Σ^+ decay modes and two kinematic solutions per decay mode); for the Σ^- events, there may be up to two points plotted per event (two kinematic solutions for the Σ^- decay).

B. Data Analysis

1. Scanning, Measuring, Reconstruction, and Kinematic Fitting

The reactions studied in this paper appear in the bubble chamber as two-prong or four-prong topologies with a charged decay, or "kink," on the hyperon track. In Ref. 13 there is a detailed account of the scanning and measuring techniques, spatial reconstruction, and kinematic fitting procedures, and a detailed study of $\Sigma^\pm$ detection efficiencies as they apply to the reactions $K^-p \to \Sigma^\pm\pi^\mp$ from this exposure. These discussions also apply to the reactions studied in this paper. The $\Sigma^\pm$ detection weighting procedures developed in Ref. 13 were used in this paper only to compute cross sections and in the analysis of reaction (1).

2. Event Selection; Four-Constraint Hypotheses

Reactions (3)–(6) have four kinematic constraints, since the vector momenta of all charged tracks are measured.[14] Consequently, these hypotheses can nearly always be selected uniquely by means of kinematic fitting alone. Except for the ambiguity decisions discussed below, events for these reactions were accepted for further study whenever the χ^2 probability exceeded 0.02 and the Σ lifetime was less than five mean lifetimes.

There are three classes of possible ambiguity in interpretation for reactions (3)–(6):

(a) An ambiguity between Σ^+ decay modes for reactions (3) or (5) occurred for about 2% of the events; however, in every case this ambiguity was resolved by a track-density estimate for the charged decay product.

(b) For successful fits to (5) or (6), a successful fit to (7) or (8) nearly always was found as well. However, in every case where track-density estimates could be used, hypotheses (5) or (6) were favored. An inspection of the ambiguous fits to (7) and (8) indicated that the fitting program could usually conserve energy and momentum by replacing the K^+K^- pair with a $\pi^+\pi^-$ pair and by adding a low momentum π^0 which travels along the beam direction. Therefore, we ruled in favor of reactions (5) or (6) whenever the χ^2 probability exceeded 0.02.

(c) Another ambiguity occurred for reactions (5) and (6) due to the interchange of the π and K particles of the same charge in situations where the two travel roughly in the same direction with momenta sufficiently high so that track density information is not useful. These conditions were met for about 10% of the events fitting (5) or (6); in these cases the hypothesis with the highest χ^2 probability was chosen.

3. Event Selection; One-Constraint Hypotheses

Reactions (1), (2), (7), and (8) have one kinematic constraint since the vector momentum of the π^0 is not measured. Selection of one-constraint hypotheses is generally a difficult problem. A number of factors may cause difficulties in interpretation; in this experiment, the main problem is with the momentum measurement of the Σ track. Although the outgoing baryon track is generally identified by the kink signature together with track-density and lifetime information, the vector momentum of the Σ is not always well determined.[14] Short Σ tracks tend to have large uncertainties (for example, a 1.0-cm Σ track typically has a 10% uncertainty in magnitude of momentum); two kinematic solutions for the Σ momentum are often available; for Σ^+ events, two decay modes are possible. Thus there are up to four (two) possible Σ^+ (Σ^-) momenta at the start of kinematic fitting, each of which may have a large uncertainty.

First consider reactions (1) and (2). Figure 1 shows distributions for the square of the invariant missing mass (MM^2) defined simply as

$$\mathrm{MM}^2 = (P_{K^-} + P_p - \sum_{i=1}^{n} P_i)^2,$$

where the P's are the four-vectors of the event, and there are n charged outgoing particles. Events with a four-constraint fit to $K^-p \to \Sigma^\pm\pi^\mp$ have been removed;

[13] J. S. Loos, U. E. Kruse, and E. L. Goldwasser, Phys. Rev. 173, 1330 (1968).

[14] Usually the Σ track is too short and straight to measure for curvature. In such cases, the Σ momentum at the production vertex is provided by a preliminary calculation of energy-momentum balance at the decay vertex followed by a "swimming" procedure to correct for changes in energy and direction incurred in traveling to the decay point. The decay calculation yields two solutions (not necessarily both are physical) for the Σ momentum.

the remaining Σ^+ (Σ^-) events have up to four (two) points each, for the reasons stated above. Clearly, there are large backgrounds of "missing-mass" hypotheses under rather broad π^0 bands. The shaded events are those which have been classified as reactions (1) or (2) by our selection criteria given below. Statistically, at least, the selection criteria seem to provide a reasonably clean sample of events since the unshaded backgrounds under the pion bands appear consistent with neighboring background regions. The following selection criteria were used to classify the events as reactions (1) or (2):

(a) χ^2 probability greater than 0.05,

(b) track density estimates consistent with hypothesis,

(c) $-(\delta\mathrm{MM}^2+2m_\pi{}^2)\leq(\mathrm{MM}^2-m_\pi{}^2)\leq(\delta\mathrm{MM}^2+2m_\pi{}^2)$,

and

(d) $\delta\mathrm{MM}^2\leq 20m_\pi{}^2$,

where $\delta\mathrm{MM}^2$ is the estimated uncertainty in MM^2. As a check on these selection criteria, a sample of 200 events from reactions (3) and (4) were refitted as reactions (1) and (2) by ignoring the presence of a π^+ and a π^- track. Nearly 30% of the events satisfied (a) and (b), 20% satisfied (a)–(c), but only 5% satisfied (a)–(d). Thus the combination of the four criteria is quite effective in removing spurious missing-mass hypotheses. We estimate that losses to or contamination from missing-mass reactions is 15% or less for reaction (1), and 30% or less for reaction (2) (the higher contamination of the latter is simply the result of a smaller true signal in that channel).

Another possible source of contamination to reactions (1) and (2) are the reactions $K^-p\to\Sigma^{\pm}K^{\mp}K^0$ (K^0 unseen). However, an examination of such events in this exposure which have a visible K^0 decay and four kinematic constraints leads to the conclusion that this contamination is negligible.[15]

The selection of events for reactions (7) and (8) is similar to that for reactions (1) and (2). Figure 2 shows distributions for MM^2 after removing all events with four-constraint fits to (3)–(6). Also removed from Fig. 2(a) are events associated with the $\Sigma^+\to p\pi^0$ decay mode, where the decay proton is identified by track density. The latter events have been removed because they are not studied in this paper. The shaded events are those identified by criteria (a)–(c) above, and by

$$(d')\ \delta\mathrm{MM}^2\leq 16m_\pi{}^2.$$

The unshaded backgrounds under the pion peaks appear consistent with neighboring regions for both (7) and (8). We estimate that losses to or contamination from missing-mass reactions is less than 10% for reactions (7) and (8).

[15] In the entire sample of film, there were only 28 events identified as $\Sigma^{\pm}K^{\mp}K^0$, $K^0\to\pi^+\pi^-$. Only two of these events satisfied the selection criteria for $\Sigma^{\pm}\pi^{\mp}\pi^0$. There were 40 events identified as either $\Sigma^{\pm}K^{\mp}\pi^+\pi^-K^0$ or $\Sigma^{\pm}K^{\pm}\pi^{\mp}\pi^{\mp}K^0$, $K^0\to\pi^+\pi^-$. Only three of these events satisfied the selection criteria for $\Sigma^{\pm}\pi^{\mp}\pi^+\pi^-\pi^0$. We would like to thank P. F. Schultz of the University of Illinois for making this information available.

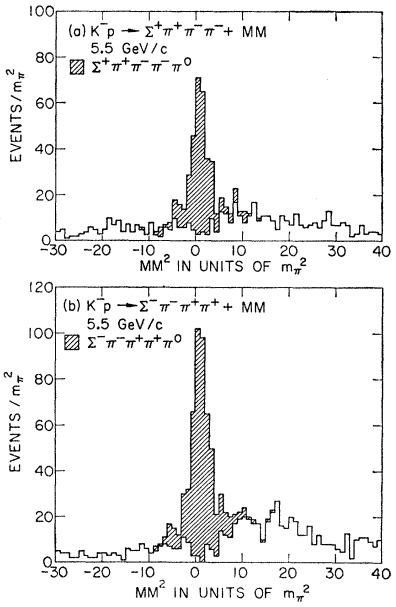

FIG. 2. Distribution of MM^2 for the (four-prong plus kink) events. (a) $K^-p\to\Sigma^+\pi^-\pi^+\pi^-+\mathrm{MM}$, $\Sigma^+\to\pi^+n$; (b) $K^-p\to\Sigma^-\pi^+\pi^+\pi^-+\mathrm{MM}$, $\Sigma^-\to\pi^-n$. The shaded events are those which have been selected as one-constraint fits with an unseen π^0. Four-constraint events ($K^-p\to\Sigma^{\pm}\pi^{\mp}\pi^+\pi^-$ or $\Sigma^{\pm}\pi^{\mp}K^+K^-$) have been omitted. In addition, we have removed events associated with the decay mode $\Sigma^+\to p\pi^0$, where the decay proton is identified by track density. There may be up to two points per event since there are two kinematic solutions for the Σ decay.

The reactions $K^-p\to\Sigma^{\pm}K^{\mp}\pi^+\pi^-K^0$ (K^0 unseen), $K^-p\to\Sigma^{\pm}K^{\pm}\pi^{\mp}\pi^{\mp}K^0$ (K^0 unseen), or $K^-p\to\Sigma^{\pm}\pi^{\mp}K^+K^-\pi^0$ constitute negligible contaminations to (7) and (8), as verified by an examination of events from this exposure having visible K^0 decays and four kinematic constraints.[15]

III. EXPERIMENTAL RESULTS AND DISCUSSION

A. Final-State Cross Sections

The final-state cross sections for reactions (1)–(8) at 5.5 GeV/c are presented in Table I. For Σ^+ reactions the cross sections were compiled using only the $\Sigma^+\to\pi^+n$ decay mode, since events associated with the $\Sigma^+\to p\pi^0$ mode are unreliably detected when the Σ^+

TABLE I. Final-state cross sections.

Final state	No. obs. events[a]	Corr. cross section (μb)
$\Sigma^+\pi^-\pi^0$	150	130±18
$\Sigma^-\pi^+\pi^0$	73	30± 7
$\Sigma^+\pi^-\pi^+\pi^-$	188	135±16
$\Sigma^-\pi^+\pi^+\pi^-$	218	79± 9
$\Sigma^+\pi^-K^+K^-$	43	31± 6
$\Sigma^-\pi^+K^+K^-$	59	20± 4
$\Sigma^+\pi^-\pi^+\pi^-\pi^0$	325	250±25
$\Sigma^-\pi^+\pi^+\pi^-\pi^0$	505	190±20

[a] For Σ^+ final states, only events with $\Sigma^+\to\pi^+n$ decays have been used for cross-section determination; a factor of 2 has been applied to correct for the omission of the other Σ^+ decay mode.

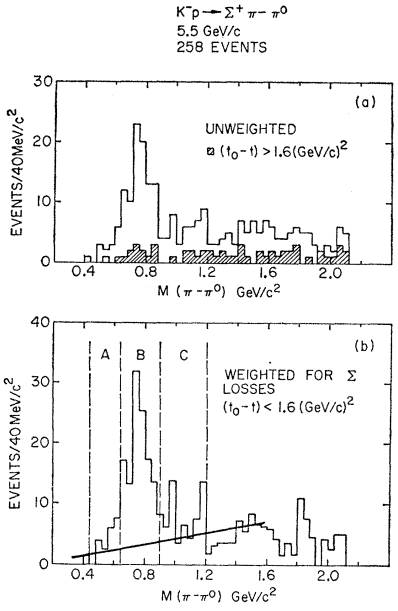

FIG. 3. Invariant-mass spectrum for $(\pi^-\pi^0)$ from $K^-p \to \Sigma^+\pi^-\pi^0$. (a) Observed spectrum, with no weighting due to Σ^+ detection efficiency. For the shaded events, the square of the momentum transfer from the K^- to the $(\pi^-\pi^0)$ system exceeds 1.6 $(\mathrm{GeV}/c)^2$. The nonperipheral events are seen to contribute only a very small signal to the $\rho^0(770)$. (b) Spectrum weighted for Σ^+ detection efficiency for events having a momentum transfer squared less than 1.6 $(\mathrm{GeV}/c)^2$. The solid line is a rough estimate of background. Regions A, B, and C, respectively, are defined by the following $M(\pi^-\pi^0)$ intervals: 0.440–0.640 GeV/c^2, 0.640–0.900 GeV/c^2, and 0.900–1.200 GeV/c^2.

laboratory momentum is in excess of about 1.0 GeV/c. The cross-section values are corrected for Σ detection efficiency according to prescriptions developed in Ref. 13; the average detection weight factor varies from 1.2 for reaction (6) to 1.4 for reaction (1). Additional allowances have been made for the χ^2 probability cuts (2–5%), for the Σ lifetime cut (1%), and for measurement failures (3%). The uncertainties given are larger than the statistical uncertainties in order to allow for possible systematic errors in event selection, Σ detection efficiencies, or total K^- track length.

B. Reaction $K^-p \to \Sigma^+\pi^-\pi^0$

Our discussion of this reaction is limited to the $\Sigma^+\rho^-$ channel where a clean, peripherally produced signal is observed. The peripheral character of this channel causes the laboratory Σ^+ momentum distribution to peak well below 1.0 GeV/c; this fact permits the use of events from both Σ^+ decay modes without the problem of severe detection bias. The distributions of interest are then weighted for Σ^+ detection efficiency according to the prescription of Ref. 13.

A strong $\rho^-(770)$ signal is seen in Fig. 3(a), the $(\pi^-\pi^0)$ invariant-mass distribution for all observed events (unweighted for Σ^+ detection loss). The nonperipheral events (shaded), however, do not show a significant ρ^- signal. Therefore, we consider only those events with (t_0-t) less than 1.6 $(\mathrm{GeV}/c)^2$, where t is

TABLE II. Differential cross section for $K^-p \to \Sigma^+\rho^-$ at 5.5 GeV/c.

(t_0-t) interval $(\mathrm{GeV}/c)^2$	No. obs. events	No. corr. events	$d\sigma/dt$ $[\mu\mathrm{b}/(\mathrm{GeV}/c)^2]$
0.0–0.1	11	26.2±11.9	68±32
0.1–0.2	16	27.4±10.3	74±28
0.2–0.3	9	17.4± 8.7	47±23
0.3–0.4	12	20.0± 8.7	54±23
0.4–0.6	21	28.9± 9.4	39±13
0.6–1.0	7	12.8± 7.3	8± 5
1.0–1.6	6	12.9± 8.0	6± 5

the invariant momentum transfer squared and t_0 is the kinematic maximum of t for a given $(\pi^-\pi^0)$ mass.[16] Figure 3(b) shows the $(\pi^-\pi^0)$ invariant-mass spectrum after the momentum transfer cut and after weighting for Σ^+ detection loss. The solid line is our estimate of background under the ρ^- signal. We find the cross section for $K^-p \to \Sigma^+\rho^-$ at 5.5 GeV/c to be 39 ± 10 μb.

The (t_0-t) distribution for events from regions $(A+C)$ and B of Fig. 3(b) are shown in Fig. 4. Region B is nearly pure ρ^-, whereas $(A+C)$ contains the tails of the ρ^- as well as background. Since the two samples of events have similar (t_0-t) distributions, a meaningful background subtraction is not possible. Rather, we use only the events from region B for further analysis, under the assumption that they form a clean and representative sample of $\Sigma^+\rho^-$ events. A suitable adjustment is made to allow for the omission of the ρ^- tails contained in $(A+C)$.

The differential cross section in the peripheral region is presented in Table II and plotted on a logarithmic scale in Fig. 5 (solid circles). The uncertainties are equal to the statistical uncertainties arbitrarily multiplied by 1.5 in order to allow for possible inaccuracies in event selection or in Σ^+ detection efficiencies. There appears to be a flattening of the differential cross section as (t_0-t) approaches zero, although the uncertainties are rather

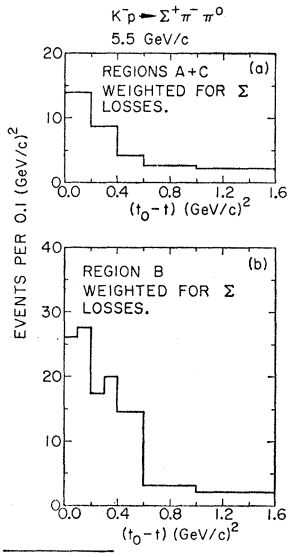

FIG. 4. Distribution for momentum transfer squared from the K^- to the $(\pi^-\pi^0)$ system. (a) Regions A+C from Fig. 3; (b) Region B from Fig. 3.

[16] In terms of the over-all c.m. momenta for the incident K^- and outgoing ρ^-: $(t_0-t)=2(|\mathbf{P}_K^-||\mathbf{P}_\rho^-|-\mathbf{P}_K^-\cdot\mathbf{P}_\rho^-)$.

large. In Fig. 5 we also show for comparison the reaction $K^-p \to \Sigma^+\pi^-$.[13] In the first bin, the mean Σ^+ momenta are 350 and 390 MeV/c for $\Sigma^+\pi^-$ and $\Sigma^+\rho^-$, respectively. The corresponding Σ^+ detection factors are 2.3 and 2.1; thus the relative Σ^+ detection efficiencies are reasonably well known.

In Fig. 6 we show the ρ^--decay angular distributions for various (t_0-t) bins. The angles θ and φ are the polar and azimuthal angles of the π^- defined in the rest frame of the ρ^- by taking the z axis along $\mathbf{P}_{K^-}$ and the y axis along $\mathbf{P}_p \times \mathbf{P}_{\Sigma^+}$, where $\mathbf{P}_{K^-}$, $\mathbf{P}_p$, and $\mathbf{P}_{\Sigma^+}$ are the indicated momenta. In the density-matrix formalism, the decay angular distribution for a vector meson decaying into two pseudoscalar mesons is given by[17]

$$W(\theta,\varphi) = (3/4\pi)[\rho_{00}\cos^2\theta + \tfrac{1}{2}(1-\rho_{00})\sin^2\theta - \rho_{1,-1}\sin^2\theta\cos 2\varphi - \sqrt{2}\,\mathrm{Re}\rho_{10}\sin 2\theta\cos\varphi].$$

Integrating over φ, then $\cos\theta$, gives

$$W(\theta) = \tfrac{3}{2}[\rho_{00}\cos^2\theta + \tfrac{1}{2}(1-\rho_{00})\sin^2\theta],$$
$$W(\varphi) = (1/2\pi)[1-2\rho_{1,-1}\cos 2\varphi].$$

Thus the strong $\sin^2\theta$ component evident in Fig. 6 indicates a small ρ_{00}, and the strong $\cos 2\varphi$ component indicates a large $\rho_{1,-1}$. The solid curves superimposed on Fig. 6 are based on the values of the density matrix elements, given in Table III, found by a moment calculation. Because of the poor statistics, some of the (t_0-t) intervals yield negative (unphysical) values for for ρ_{00}. In such cases our best estimates for both ρ_{00} and $\mathrm{Re}\rho_{10}$ are zero.

The only other report of density matrix elements in this reaction has been made for the 3.5-GeV/c data,[5]

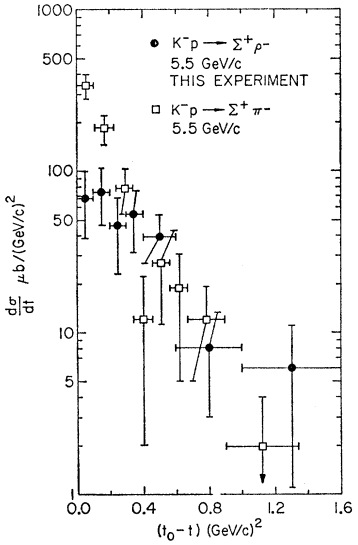

FIG. 5. Differential cross section in the peripheral region for $K^-p \to \Sigma^+\rho^-(770)$. The solid circles are the results of this experiment; the open squares are the results for the reaction $K^-p \to \Sigma^+\pi^-$ from the same exposure of film (see Ref. 13) and are included for comparison (see text).

[17] K. Gottfried and J. D. Jackson, Nuovo Cimento 33, 309 (1964).

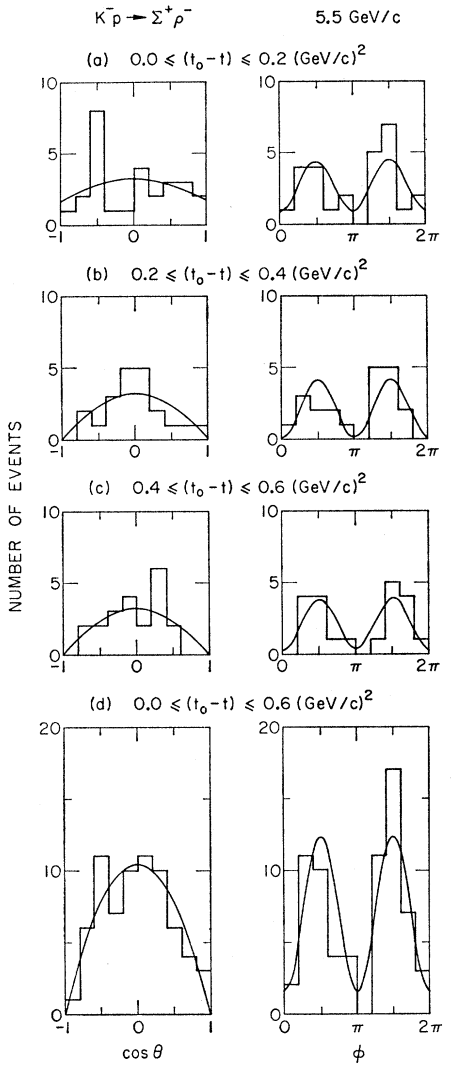

FIG. 6. Decay angular distributions in the rest frame of the $\rho^-(770)$ for the reaction $K^-p \to \Sigma^+\rho^-$. (a) $0.0 \leq (t_0-t) \leq 0.2$ (GeV/c)^2, (b) $0.2 \leq (t_0-t) \leq 0.4$ (GeV/c)^2, (c) $0.4 \leq (t_0-t) \leq 0.6$ (GeV/c)^2, and (d) $0.0 \leq (t_0-t) \leq 0.6$ (GeV/c)^2. Definitions of the polar angle θ and the azimuthal angle φ are given in the text. The distributions are not weighted for Σ^+ detection efficiency, since their shapes should be independent of such weighting. The solid curves are based on moment calculations for the decay density matrix elements (see text).

where the averaged values of ρ_{00} and $\rho_{1,-1}$ were found to be 0.17 ± 0.08 and 0.17 ± 0.08, respectively.

The character of the density matrix elements indicates that the production is dominated by natural-parity exchange, although a small contribution from pseudoscalar (K meson) exchange cannot be ruled out for small values of (t_0-t). Pure natural-parity exchange, unmodified by absorption effects, would predict values of zero for ρ_{00} and $\frac{1}{2}$ for $\rho_{1,-1}$.[17] A possible explanation for the lack of K-meson exchange is that the small value of the ΣNK coupling constant[18] suppresses this exchange relative to natural-parity exchange. However, this explanation seems unlikely because, although the ΛNK

TABLE III. Density matrix elements for $K^-p \to \Sigma^+\rho^-$ at 5.5 GeV/c.

(t_0-t) interval $(\mathrm{GeV}/c)^2$	Calculated elements[a]			Adjusted elements[b]		
	ρ_{00}	$\rho_{1,-1}$	$\mathrm{Re}\rho_{10}$	ρ_{00}	$\rho_{1,-1}$	$\mathrm{Re}\rho_{10}$
0.0–0.2	0.21±0.12	0.32±0.12	0.00±0.07	0.21±0.12	0.32±0.12	0.00±0.07
0.2–0.4	−0.12±0.11	0.47±0.14	−0.11±0.06	0.00±0.12	0.47±0.14	0.00±0.07
0.4–0.6	−0.18±0.10	0.39±0.15	−0.02±0.06	0.00±0.12	0.39±0.15	0.00±0.07
0.0–0.6	−0.01±0.07	0.39±0.08	−0.04±0.04	0.00±0.10	0.39±0.08	0.00±0.05

[a] Calculated by method of moments. [b] Adjusted to be physical.

coupling constant is large,[18] the reaction $K^-p \to \Lambda\rho^0$ at 5.5 GeV/c has a cross section of 23±8 μb (which is smaller than that for $K^-p \to \Sigma^+\rho^-$) and a value for ρ_{00} consistent with zero.[19] A more tenable explanation for the absence of K-meson exchange can be found in terms of the Regge model, where the trajectory function $\alpha(t)$ associated with the natural parity $K^*(890)$ and $K^*(1420)$ mesons are thought to lie higher than the trajectory associated with the K meson.

Arnold[20] has proposed a Regge model for vector-meson production which features the exchange of $K^*(890)$ and $K^*(1420)$ trajectories and which incorporates $SU(6)_W$ symmetry as well as $SU(3)$ symmetry for the Regge residues. The prediction made by Arnold which is of particular interest here is

$$\left[\frac{d\sigma}{dt}(K^-p \to \Sigma^+\rho^-) \Big/ \frac{d\sigma}{dt}(K^-p \to \Sigma^+\pi^-)\right]_{t=t_0} = \tfrac{2}{3}.$$

The differential cross section for $K^-p \to \Sigma^+\pi^-$ at 5.5 GeV/c, resported by the present authors in a separate publication,[13] is shown in Fig. 5 (open squares) for comparison. The $\Sigma^+\pi^-$ differential cross section is clearly peaked more forward than the $\Sigma^+\rho^-$ differential cross section. Taking the values from the smallest (t_0-t) bin, we find an experimental ratio of

$$(68\pm32)/(350\pm70) = 0.20\pm0.10.$$

Therefore, the experimental result is not in agreement with Arnold's prediction. A more elaborate Regge calculation could perhaps explain the $\Sigma^+\rho^-$ data, but the accuracy of the present experiment could probably test only its gross features.

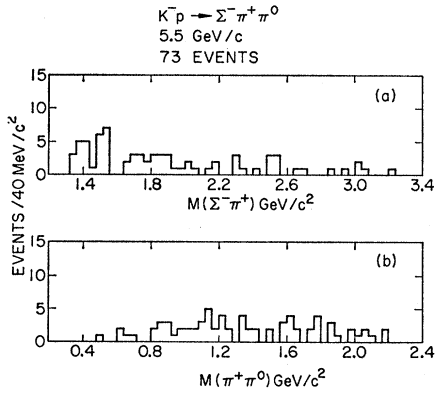

FIG. 7. Invariant-mass distributions for the reaction $K^-p \to \Sigma^-\pi^+\pi^0$. (a) Mass of the $(\Sigma^-\pi^+)$ system; (b) Mass of the $(\pi^+\pi^0)$ system.

C. Reaction $K^-p \to \Sigma^-\pi^+\pi^0$

The only significant structure observed in this reaction is in the $\Sigma^-\pi^+$ invariant-mass spectrum. This reaction is therefore well suited for studying $Y^{*0}\pi^0$

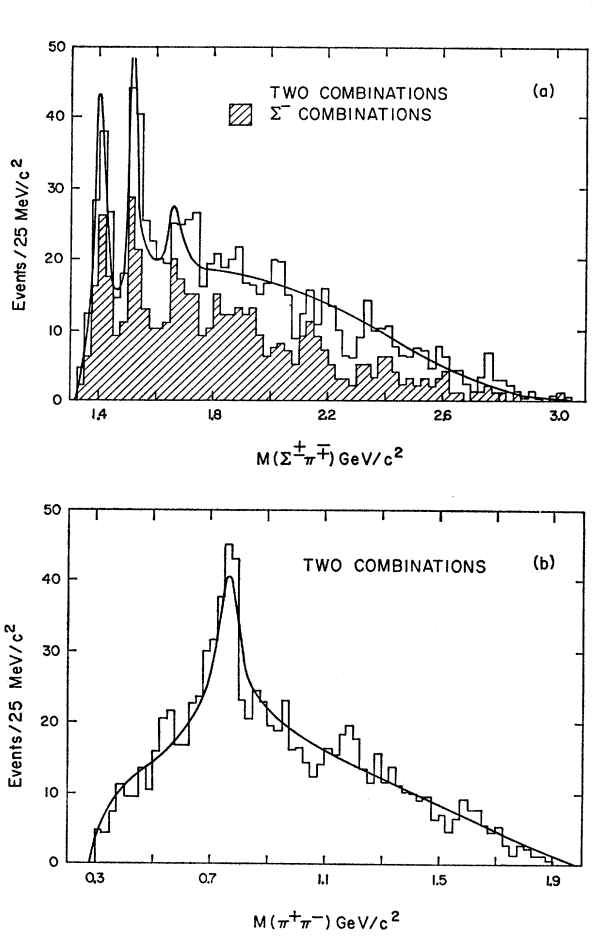

FIG. 8. Invariant-mass spectra for $(\Sigma\pi)^0$ and $(\pi\pi)^0$ from $K^-p \to \Sigma^\pm\pi^\mp\pi^+\pi^-$. (a) $\Sigma^\pm\pi^\mp$, two combinations; (b) $\pi^+\pi^-$, two combinations. The solid curves are obtained from a maximum-likelihood fit (see text).

[18] Jae Kwan Kim, Phys. Rev. Letters **19**, 1079 (1967).
[19] J. Mott, Ph.D. thesis, Northwestern University (unpublished).
[20] R. C. Arnold, Phys. Rev. **162**, 1334 (1967).

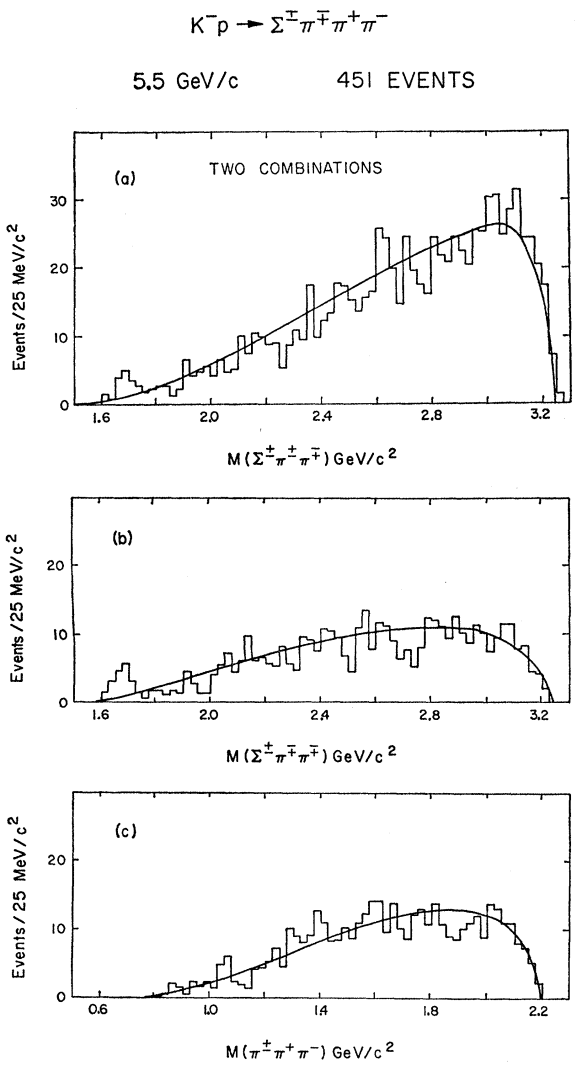

FIG. 9. Invariant-mass spectra for singly charged combinations from $K^-p \to \Sigma^{\pm}\pi^{\mp}\pi^+\pi^-$. (a) $\Sigma^{\pm}\pi^{\pm}\pi^{\mp}$, two combinations; (b) $\Sigma^{\pm}\pi^{\mp}\pi^{\mp}$; and (c) $\pi^{\pm}\pi^+\pi^-$. The solid curves are obtained from a maximum-likelihood fit (see text).

channels where the Y^* decays into $\Sigma^-\pi^+$. (The $\Sigma^+\pi^-\pi^0$ reaction, on the other hand, is complicated by the presence of a strong ρ^- resonance.) Figure 7 shows the invariant mass plots for the $\Sigma^-\pi^+$ and $\pi^+\pi^0$ combinations. There are small, but clear, $Y_0^*(1405)$ and $Y_0^*(1520)$ signals. In Figs. 22(a) and 22(e) we show the c.m. production cosine distributions for the $Y_0^*(1405)\pi^0$ and $Y_0^*(1520)\pi^0$ channels; the $Y_0^*(1405)$ events are peripherally produced, whereas the $Y_0^*(1520)$ events fall both in the peripheral and antiperipheral regions. The cross sections for these channels, fully corrected, are given in Table VI.

D. Reactions $K^-p \to \Sigma^{\pm}\pi^{\mp}\pi^+\pi^-$

A number of channels involving resonances are observed in the reactions $Y_0^*(1405)\pi^+\pi^-$, $Y_0^*(1520)\pi^+\pi^-$, $Y^*(\sim 1665)\pi^+\pi^-$, $\Sigma^{\pm}\pi^{\mp}\rho^0(770)$, $Y_0^*(1405)\rho^0(770)$, and $Y_0^*(1520)\rho^0(770)$. We find that the quasi-three-body channels dominate the reactions, in agreement with the results found at 3.5 GeV/c.[6] Events associated with the $\Sigma^+ \to p\pi^0$ decay mode are not considered because these events are highly biased against Σ^+ particles with laboratory momenta greater than about 1.0 GeV/c.

1. *General Features of the Reactions*

The invariant-mass plots for the $(\Sigma\pi)^0$ and $(\pi\pi)^0$ combinations are shown in Fig. 8. Two combinations are plotted per event and the events from both reac-

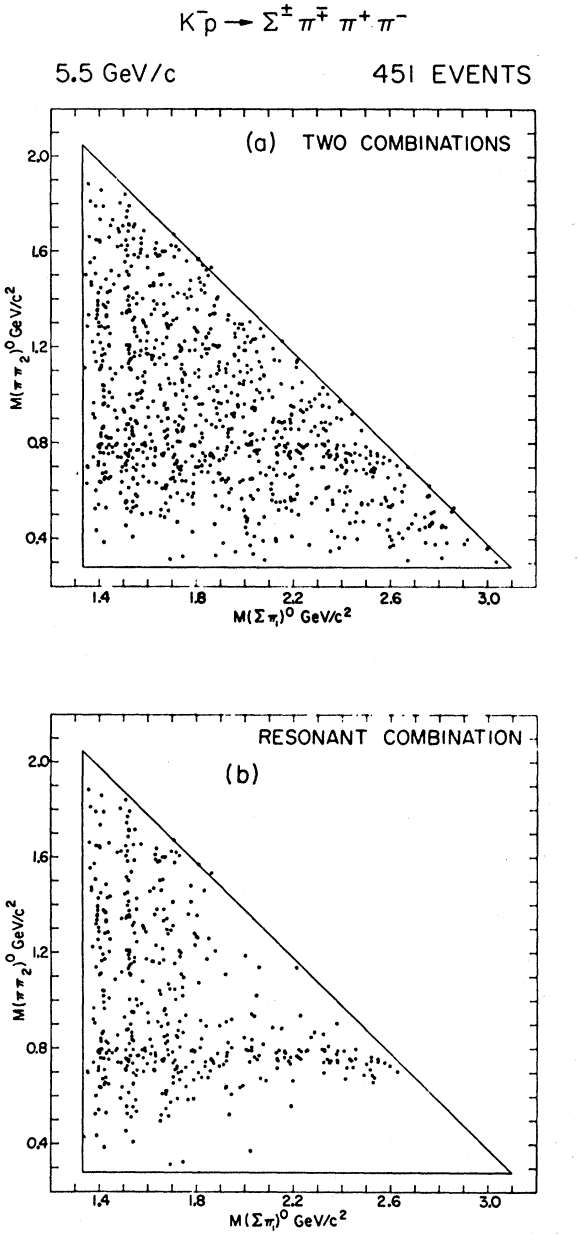

FIG. 10. Triangle plot for $(\Sigma\pi)^0$ versus $(\pi\pi)^0$ from $K^-p \to \Sigma^{\pm}\pi^{\mp}\pi^+\pi^-$. (a) Two combinations per event. (b) One combination per event, chosen to remove nonresonant combinations (see text).

tions have been added together. The $\rho^0(770)$ resonance dominates the $(\pi\pi)^0$ spectrum, while the $Y_0^*(1405)$, $Y_0^*(1520)$, and $Y^*(\sim 1665)$ are prominent features of the $(\Sigma\pi)^0$ spectrum. In Fig. 9, we show the singly charged three-particle invariant-mass spectra. The only significant structure seen is the $Y_1^*(1665)$, which shows up as a small excess of events at the low end of phase space; these events are associated with positive charge ($\Sigma^+\pi^+\pi^-$ or $\Sigma^-\pi^+\pi^+$) and small momentum transfers. The solid curves superimposed on Figs. 8 and 9 result from a maximum-likelihood fit, described below.

Figure 10(a) is a triangle plot of the invariant mass of the $(\Sigma\pi)^0$ system versus that of the $(\pi\pi)^0$ system; two combinations per event are plotted. The resonances seen in Fig. 8 are evident as bands in the triangle plot. Quasi-two-body production in $Y^*\rho^0$ channels is clearly rather small since the overlap regions do not have large populations.

We have investigated other mass distributions and mass scatter plots but have found no positive effects. In particular, no $(\Sigma\pi\pi)$ resonances decaying via $Y^*\pi$ or $\Sigma\rho^0$ were found, aside from the small $Y_1^{**}(1665)$ signal already mentioned. No enhancements in the $\rho^0\pi$ spectrum were seen, either.

2. *Technique for Maximum-Likelihood Fit to Resonance Production*

The technique used to fit the resonance production in the final state is a more or less standard one[21] which assumes a set of Breit-Wigner resonant amplitudes plus a phase-space background. The computer program MINFUN,[22] has been used to search for the maximum of the likelihood function.

If we denote the probability for the ith event by P_i, the likelihood function (for N events) has the form

$$L=\prod_{i=1}^{N} P_i,$$

where $P_1=\rho_i(\alpha_{\rm ps}R_{\rm ps}+\sum_{j=1}^{n}\alpha_j R_{ji})$, ρ_i is the phase space for the ith event, α_j is the fraction of events proceeding via the jth process, n is the number of assumed resonant processes, $\alpha_{\rm ps}\equiv 1.0-\sum_{j=1}^{n}\alpha_j=$ fraction via pure phase space, R_{ji} is the resonance function for the jth process evaluated for the ith event, and $R_{\rm ps}$ is the phase-space factor.

The function R_{ji} can be of several forms depending on the complexity assumed for the jth process. If we denote the physical variables by $\{x\}$ and the amplitude for the jth process by $A_j(x)$, then R_{ji} is defined as

$$R_{ji}=|A_j(x_i)|^2/N_j,$$

where

$$N_j=\int |A_j(x)|^2\rho(x)dx,$$

a normalization integral. For the simplest process, phase space, $R_{\rm ps}$ is computed by setting $|A|^2$ to unity. In the case of a single resonance involving particles 1 and 2, $|A|^2$ is simply a Breit-Wigner function:[23]

$$|A(M_{12})|^2=\left(\frac{M_{12}}{q_{12}}\right)\left(\frac{\Gamma}{(M_0^2-M_{12}^2)^2+M_0^2\Gamma^2}\right),$$

where M_{12} is the invariant mass of particles 1 and 2, q_{12} is the momentum of particle 1 in rest frame of (1,2), M_0 is the resonant mass, $\Gamma=\Gamma_0(q_{12}/q_0)^{2l+1}$, Γ_0 is the partial width of the resonance, $q_0=q_{12}$, evaluated when $M_{12}=M_0$, and l is the orbital angular momentum of decay.

In the case of double resonance production in which particles 1 and 2 are resonant at the same time that particles 3 and 4 are resonant, $|A|^2$ may be expressed as a product of two Breit-Wigner amplitudes (each with its own resonance parameters)

$$|A(M_{12},M_{34})|^2=|A(M_{12})|^2|A(M_{34})|^2.$$

The four-body phase space factor ρ may be expressed in terms of a product of two-body factors

$$\rho(M_{12},M_{34})dM_{12}^2\,dM_{34}^2=C\left(\frac{q_{12}}{M_{12}}\right)\left(\frac{q_{34}}{M_{34}}\right)\left(\frac{q}{E_{\rm c.m.}}\right)dM_{12}^2\,dM_{34}^2,$$

where q_{12}, q_{34}, M_{12}, and M_{34} are defined above, q is the momentum of system (1,2) in the over-all c.m., and $E_{\rm c.m.}$ is the c.m. energy. The normalization integral for the jth process for either single or double resonance production is conveniently expressed in terms of the factored form of ρ

$$N_j=\int\int |A_j(M_{12},M_{34})|^2\rho(M_{12},M_{34})dM_{12}^2\,dM_{34}^2.$$

3. *Resonance Fractions as Found by Maximum-Likelihood Method A*

The data indicate dominance of quasi-three-body production for the $\Sigma\pi\pi\pi$ final state; therefore, as a first fit for resonance production, only the presence of the $Y^*\pi^+\pi^-$ and $\Sigma^\pm\pi^\mp\rho^0(770)$ channels was assumed. During the calculation, the positions and widths of the assumed states were held fixed at the following values: neutral Y^* resonances at 1405, 1520, and 1665 MeV/c^2 with widths of 40, 20, and 45 MeV/c^2, respectively; neutral ρ meson at 770 MeV/c^2 with a width of 120 MeV/c^2. The problem of two identical pions, π_a and π_b, was handled by averaging the resonant function over the two possible combinations

$$|A_j|^2=\tfrac{1}{2}[|A_j(M_a)|^2+|A_j(M_b)|^2],$$

where $M_{a,b}$ is the invariant mass formed by $(\Sigma\pi_{a,b})$ or $(\pi\pi_{a,b})$.

[21] J. Friedman and R. Ross, Alverez Group Programmers Note No. P-102, Lawrence Radiation Laboratory, 1964 (unpublished).

[22] W. E. Humphrey, Alverez Group Programmers Note No. P-6, Lawrence Radiation Laboratory, 1962 (unpublished).

[23] J. D. Jackson, Nuovo Cimento 34, 1644 (1964).

The results of the fit are presented in Table IV. The numbers given are the percentages of all events which appear in the various processes and the uncertainties are equal to the square roots of the diagonal elements of the variance matrix obtained in the fit.

A visual display of the fit is provided by the solid curves superimposed on the invariant-mass plots of Figs. 8 and 9. These curves were produced by the use of a Monte Carlo event generating routine GENEV.[24] The resonance shapes appear as a consequence of weighting each Monte Carlo event by the factor

$$P_i=\rho_i(\alpha_{\rm ps}R_{\rm ps}+\sum_{j=1}^{n}\alpha_j R_{ji})$$

in the notation of the previous section. The values of α_j used here, of course, are those found in the maximum-likelihood fit. Generally speaking the curves adequately represent the data. It is not too surprising that the $Y^*(\sim 1665)$ enhancement peaks above 1665 MeV/c^2, since there are several other resonances in this mass region.[25–28] A small $Y_1^*(1665)$ signal in the $(\Sigma\pi\pi)$ channel is apparent and there is also a slight excess of events in the f_0 region of the $(\pi\pi)^0$ spectrum.

4. *Resonance Fractions as Found by Maximum-Likelihood Method B*

The results of the preceding section indicate that more than 75% of the events in the $\Sigma\pi\pi\pi$ final state are produced as quasi-three-body final states. Yet there is a large false background due to two combinations for the $(\Sigma\pi)^0$ and $(\pi\pi)^0$ pairs. Presumably, for any given event only one of the two identical pions is associated with the $(\Sigma\pi)^0$ or $(\pi\pi)^0$ resonance. Since we know which resonances are produced in this reaction, the question arises as to whether a reasonable *a posteriori* choice between the two identical pions can be made.

The question, explicitly stated, is the following: Given a combination of particles $\Sigma\pi\pi_a\pi_b$, where π_a and π_b are identical, which of the following two sets of mass combinations should we plot:

$$\text{set 1: } (\Sigma\pi_a)^0,\ (\pi\pi_b)^0,\ (\Sigma\pi\pi_a)^{\pm}$$

or

$$\text{set 2: } (\Sigma\pi_b)^0,\ (\pi\pi_a)^0,\ (\Sigma\pi\pi_b)^{\pm}?$$

To make this choice for the ith event, we proceeded as follows: First, R_{ji} values for all j resonances were computed for set 1, where $R_{ji}(1)_{\rm max}$ denotes the maximum of these values. Similarly, the R_{ji} values for set 2 were found. Then set 1 was chosen whenever $R_{ji}(1)_{\rm max}$ exceeded $R_{ji}(2)_{\rm max}$, and vice versa.

This prescription was applied to the data in an effort to separate the "resonant" from the "nonresonant" combinations in $(\Sigma\pi)^0$, $(\pi\pi)^0$, and $(\Sigma^{\pm}\pi^{\pm}\pi^{\mp})$. No other mass combinations were affected. Figure 11 shows the separated mass plots and Fig. 10(b) shows the triangle plot for the resonant combination. The separation appears to be surprisingly good, although small dips do appear in the nonresonant distributions as a result of incorrectly placing some of these events into a resonant category. These misassigned nonresonant events appear to contribute only small contaminations (of the order of 10% or less) to the distributions of resonant combinations. We emphasize that in Figs. 11 and 10(b) each event is plotted exactly once; none has been removed and none has been plotted twice.

In making a second maximum-likelihood fit for resonance fractions, we used only the resonant mass combinations. That is, instead of averaging over the amplitudes for both combinations (see preceding section), the set of resonant amplitudes $\{A_j(1)\}$ was chosen whenever $R_{ji}(1)_{\rm max}$ exceeded $R_{ji}(2)_{\rm max}$, and vice versa. Some quasi-two-body $Y^*\rho^0$ processes were assumed in addition to the quasi-three-body processes assumed before. In the fit, the masses and widths for the resonances were held fixed at the same values as before.

The results of the second maximum-likelihood fit are given in Table V. The numbers given are percentages of all events produced by means of the indicated process and the uncertainties are equal to the square root of the diagonal elements of the variance matrix obtained in

TABLE IV. Resonance fractions for $\Sigma^{\pm}\pi^{\mp}\pi^{+}\pi^{-}$ by method *A*.[a]

Process[b]	Resonance fraction, α (%)
$Y_0^*(1405)\pi^+\pi^-$	17.2±2.5
$Y_0^*(1520)\pi^+\pi^-$	18.1±2.9
$Y^*(\sim 1665)\pi^+\pi^-$	6.7±3.0
$\Sigma^{\pm}\pi^{\mp}\rho^0(770)$	33.4±4.6

[a] These results are not corrected for the observed $Y_1^*(1665)^+\pi^-$ production [with $Y_1^*(1665)$ decay via $\Sigma\pi\pi$].
[b] All Y^* resonances listed decay via $\Sigma^{\pm}\pi^{\mp}$.

TABLE V. Resonance fractions for $\Sigma^{\pm}\pi^{\mp}\pi^{+}\pi^{-}$ by method *B*.[a]

Process[b]	Resonance fraction, α(%)
$Y_0^*(1405)\pi^+\pi^-$	17.2±2.6
$Y_0^*(1520)\pi^+\pi^-$	20.6±3.2
$Y^*(\sim 1665)\pi^+\pi^-$	14.1±3.1
$\Sigma^{\pm}\pi^{\mp}\rho^0(770)$	31.7±4.1
$Y_0^*(1405)\rho^0(770)$	6.5±2.3
$Y_0^*(1520)\rho^0(770)$	5.0±2.6
$Y^*(\sim 1665)\rho^0(770)$	4.7±3.3

[a] These results are not corrected for the observed $Y_1^*(1665)^+\pi^-$ production [with $Y_1^*(1665)$ decay via $\Sigma\pi\pi$].
[b] All Y^* resonances listed decay via $\Sigma^{\pm}\pi^{\mp}$.

[24] G. R. Lynch, CERN/TC/Prog. No. 64-18, 1964 (unpublished).
[25] J. D. Davies, J. D. Dowell, P. M. Hattersley, R. J. Homer, A. W. O'Dell, A. A. Carter, K. F. Riley, R. J. Tapper, D. V. Bugg, R. S. Gilmore, K. M. Knight, D. C. Salter, G. H. Stafford, and E. J. N. Wilson, Phys. Rev. Letters **18**, 62 (1967).
[26] D. Berley, P. L. Connolly, E. L. Hart, D. C. Rahm, D. L. Stonehill, B. Thevenet, W. J. Willis, and S. S. Yamamoto, Phys. Rev. Letters **15**, 641 (1965).
[27] M. Derrick, T. Fields, J. Loken, R. Ammar, R. E. P. Davis, W. Kropac, J. Mott, and F. Schweingruber, Phys. Rev. Letters **18**, 266 (1967).
[28] CERN-Heidelberg-Saclay Collaboration, Phys. Letters **24**, 198 (1967).

TABLE VI. Cross sections for two- and three-body reactions.

Reaction	Final state studied	No. events observed[a]	Corrected cross section, μb: Unadjusted for branching ratios	Corrected cross section, μb: Adjusted for branching ratios[b]
$\Sigma^+\rho^-(770)$	$\Sigma^+\pi^-\pi^0$	90[c]	39 $\pm$10	39$\pm$10
$Y_0^*(1405)\pi^0$	$\Sigma^-\pi^+\pi^0$	12	4 $\pm$ 2	12$\pm$ 6
$Y_0^*(1520)\pi^0$	$\Sigma^-\pi^+\pi^0$	12	4 $\pm$ 2	26$\pm$13
$Y_0^*(1405)\rho^0(770)$	$\Sigma^\pm\pi^\mp\pi^+\pi^-$	23	14 $\pm$ 8	21$\pm$12
$Y_0^*(1520)\rho^0(770)$	$\Sigma^\pm\pi^\mp\pi^+\pi^-$	20	11 $\pm$ 7	32$\pm$21
$Y_1^*(1665)^+\pi^-$	$\Sigma^\pm\pi^\mp\pi^+\pi^-$	18	9 $\pm$ 4	36$\pm$16[d]
$Y_0^*(1405)\pi^+\pi^-$	$\Sigma^\pm\pi^\mp\pi^+\pi^-$	54	31 $\pm$ 7	46$\pm$10
$Y_0^*(1520)\pi^+\pi^-$	$\Sigma^\pm\pi^\mp\pi^+\pi^-$	84	44 $\pm$ 9	130$\pm$27
$\Sigma^+\pi^-\rho^0(770)$	$\Sigma^+\pi^-\pi^+\pi^-$	73	46 $\pm$10	46$\pm$10
$\Sigma^-\pi^+\rho^0(770)$	$\Sigma^-\pi^+\pi^+\pi^-$	59	18 $\pm$ 5	18$\pm$ 5
$Y_0^*(1405)\omega^0(783)$	$\Sigma^\pm\pi^\mp\pi^+\pi^-\pi^0$	25	13 $\pm$ 5	21$\pm$ 8
$Y_0^*(1520)\omega^0(783)$	$\Sigma^\pm\pi^\mp\pi^+\pi^-\pi^0$	22	11 $\pm$ 4	40$\pm$15
$\Sigma^+\pi^-\omega^0(783)$	$\Sigma^+\pi^-\pi^+\pi^-\pi^0$	60	30 $\pm$10	33$\pm$11
$Y_0^*(1405)\varphi^0(1020)$	$\Sigma^\pm\pi^\mp K^+K^-$	11	5 $\pm$ 3	15$\pm$ 8
$Y_0^*(1520)\varphi^0(1020)$	$\Sigma^\pm\pi^\mp K^+K^-$	4	1.5$\pm$ 1.5	10$\pm$10

[a] Unless otherwise indicated, only events with $\Sigma^\pm \to \pi^\pm n$ decays are included; a factor of 2 has been app ied to correct for omission of $\Sigma^+ \to p\pi^0$ mode.
[b] Arthur H. Rosenfeld, Naomi Barash-Schmidt, Angela Barbaro-Galtieri, Leroy R. Price, Paul Söding, Charles G. Wohl, Matts Roos, and William J. Willis, Rev. Mod. Phys. **40**, 77 (1968).
[c] Both Σ^+ decay modes included.
[d] See Ref. 8.

the fit. Within the uncertainties, the results of this fit are consistent with those of the first fit with the exception of the $Y^*(\sim 1665)\pi^+\pi^-$ channel.

Monte Carlo curves corresponding to the parameters of the second fit are superimposed on Fig. 11. The curves appear to represent the data adequately. Note the peaking at the high end of the $(\Sigma^\pm\pi^\pm\pi^\mp)$ spectrum in the combination which excludes $(\Sigma\pi^0)$ resonances [Fig. 11(e)]. This peaking is due primarily to the reflections of the $Y_0^*(1405)$ and $Y_0^*(1520)$ resonances.

The cross sections for the various channels observed in the reaction $K^-p \to \Sigma^\pm\pi^\mp\pi^+\pi^-$ are presented in Table VI. The values given are based on the results of the second maximum-likelihood fit corrected for the presence of a small $Y_1^*(1665)^+\pi^-$ signal. This signal is readily identified in the $\Sigma\pi\pi$ spectrum because phase space is small and the production is very peripheral. A subtraction has been made from the $Y_0^*(1405)\pi^+\pi^-$ and the $Y_0^*(1404)\rho^0$ channels to correct for the decay $Y_1^*(1665)^+ \to Y_0^*(1405)\pi^+$. The uncertainties given in Table VI pertaining to this reaction are equal to the statistical errors of Table V arbitrarily multiplied by a factor of 1.5 to allow for possible limitations in the maximum-likelihood method.

TABLE VII. Some upper limits on production cross sections for high-mass hyperon resonances.[a]

Resonance	Final-state configuration[b]	Production cross section upper limit (μb)
$Y_1^*(1910)$	A	$\lesssim$ 5
	B	$\lesssim$ 5
$Y_1^*(2040)$	A	$\lesssim$10
	B	$\lesssim$ 5
$Y_0^*(2100)$	A	$\lesssim$ 5
$Y_1^*(2260)$	A	$\lesssim$ 5
	B	$\lesssim$ 5
$Y_0^*(2340)$	A	$\lesssim$10
$Y_1^*(2450)$	A	$\lesssim$ 5
	B	$\lesssim$ 5
$Y_1^*(2600)$	A	$\lesssim$ 5
	B	$\lesssim$10

[a] This table is compiled only from the $\Sigma^\pm\pi^\mp\pi^+\pi^-$ final state. Evidence for the Y^* resonances has been sought in the $(\Sigma\pi)^0$ and $(\Sigma\pi\pi)^+$ combinations.
[b] Configuration A is $Y^{*0}\pi^+\pi^-$; configuration B is $Y^{*+}\pi^-$.

5. *Search for High-Mass Hyperon Resonances*

Recently, several Y^* resonances have been discovered in the mass region above 1900 MeV/c^2.[2,25,29–31] Their masses and widths in MeV/c^2 are approximately (1910, 65), (2040, 150), (2100, 150), (2260, 180), (2340, 105), (2450, 140), and (2600, 140). The three lower-mass resonances are thought to have small branching ratios ($\sim$5%) into $\Sigma\pi$.[28] We see no evidence for any of these or any other new resonances in the $\Sigma\pi$ or $\Sigma\pi\pi$ combinations from our data; as mentioned in Sec. III D 1, no significant $Y^*\pi$ or $\Sigma\rho^0$ enhancements were found. In Table VII we give upper limits on production cross sections for these resonances as observed in the $\Sigma^\pm\pi^\mp\pi^+\pi^-$ final state.

6. *Quasi-Two-Body Production: $Y_0^*\rho^0$*

The results of the second maximum-likelihood fit (Table V) indicate that the $Y_0^*(1405)\rho^0(770)$ and $Y_0^*(1520)\rho^0(770)$ channels are very weak, and perhaps consistent with zero. Nevertheless, we show in Figs.

[29] R. J. Cool, G. Giacomelli, T. F. Kycia, B. A. Leonic, K. K. Li, A. Lundby, and J. Teigers, Phys. Rev. Letters **16**, 1228 (1966).
[30] C. G. Wohl, F. T. Solmitz, and M. L. Stevenson, Bull. Am. Phys. Soc. **10**, 529 (1965); Phys. Rev. Letters **17**, 107 (1966).
[31] R. J. Abrams, R. L. Cool, G. Giacomelli, T. F. Kycia, B. A. Leonic, K. K. Li, and D. N. Michael, Phys. Rev. Letters **19**, 678 (1967).

22(b) and 22(f) the c.m. production angular distributions for the events in the overlap regions of Fig. 10(b) (therefore, the only "resonant combination" is selected). The selection criteria on masses are the following: ρ^0 meson: $0.670 \leq M(\pi\pi)^0 \leq 0.870$ GeV/c^2, $Y_0^*(1405)$: $1.350 \leq M(\Sigma\pi)^0 \leq 1.460$ GeV/c^2 and $M(\Sigma\pi\pi)^+ \geq 1.720$ GeV/c^2 to remove the $Y_1^*(1665)^+\pi^-$ events, and $Y_0^*(1520)$: $1.490 \leq M(\Sigma\pi)^0 \leq 1.550$ GeV/c^2. The $Y_0^*(1405)\rho^0(770)$ events are seen to be peripherally produced, whereas the $Y_0^*(1520)\rho^0(770)$ events seem to have a much less peripheral character.

7. *Quasi-Three-Body Production: $Y_0^*\pi^+\pi^-$ and $\Sigma^{\pm}\pi^{\mp}\rho^0$*

Much interest, both theoretical and experimental, has recently developed in multiperipheral models for many-body final states.[32–44] Since the $\Sigma\pi\pi\pi$ final states seem to be dominated by quasi-three-body channels, it is of interest to investigate possible production mechanisms for these channels. At 5.5 GeV/c, the energy may be too low for rigorous application of such multiperipheral models, but at least a qualitative understanding may be possible.

In selecting the quasi-three-body events, only the masses of the resonant combination were considered, and the following criteria used for the channel indicated:

$Y_0^*(1405)\pi^+\pi^-$: $1.350 \leq M(\Sigma\pi)^0 \leq 1.460$ GeV/c^2,
$M(\Sigma\pi\pi)^+ \geq 1.720$ GeV/c^2,
$M(\pi\pi)^0 \leq 0.670$ or ≥ 0.870 GeV/c^2.

$Y_0^*(1520)\pi^+\pi^-$: $1.490 \leq M(\Sigma\pi)^0 \leq 1.550$ GeV/c^2,
$M(\pi\pi)^0 \leq 0.670$ or ≥ 0.870 GeV/c^2.

$\Sigma^{\pm}\pi^{\mp}\rho^0(770)$: $0.670 \leq M(\pi\pi)^0 \leq 0.870$,
$M(\Sigma\pi)^0 \geq 1.730$ GeV/c^2.

These criteria are designed to exclude quasi-two-body final states.

The production features of the $Y_0^*(1405)\pi^+\pi^-$ events are illustrated in Fig. 12. The scatter plots of the longitudinal momentum versus the transverse momentum (defined with respect to the incident K^- direction in the over-all c.m. system) have some very interesting qualitative properties. The $Y_0^*(1405)$ is generally produced in the backward direction, the π^- in the forward direction, and the π^+ "at rest" in the over-all c.m. system. Such a state of affairs could be explained by the dominance of a multiperipheral diagram such as in Fig. 16(a). Both exchanges, e_1 and e_2, must carry strangeness, and e_1 cannot be pseudoscalar.

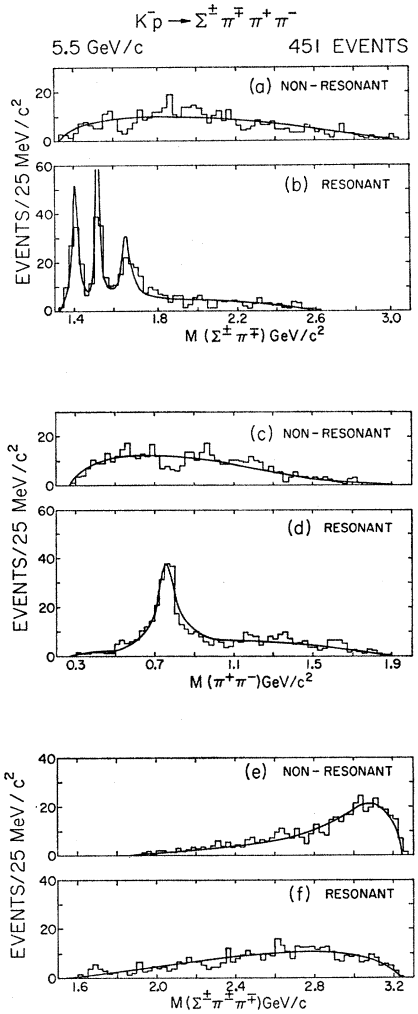

FIG. 11. Invariant-mass plots for $K^-p \to \Sigma^{\pm}\pi^{\mp}\pi^+\pi^-$ after application of separation prescription (see text): (a) $\Sigma^{\pm}\pi^{\mp}$, nonresonant combination; (b) $\Sigma^{\pm}\pi^{\mp}$, resonant combination; (c) $\pi^+\pi^-$, nonresonant combination; (d) $\pi^+\pi^-$, resonant combination; (e) $\Sigma^{\pm}\pi^{\pm}\pi^{\mp}$, combination excluding $(\Sigma\pi)^0$ resonances, (f) $\Sigma^{\pm}\pi^{\pm}\pi^{\mp}$, combination including $(\Sigma\pi)^0$ resonances. The distributions in (a) plus (b), (c) plus (d), and (e) plus (f), respectively, are equal to the distributions in Figs. 8(a), 8(b), and 9(a). The solid curves are the result of a maximum-likelihood fit (see text).

The production features of the $\Sigma^+\pi^-\rho^0$ events, shown in Fig. 13, are similar to those of the $Y_0^*(1405)\pi^+\pi^-$ channel. In this case, the Σ^+ is generally produced in the backward direction, the π^- in the forward direction, and the ρ^0 at rest in the over-all c.m. system. Again, these properties might be explained in terms of the dominance of a multiperipheral diagram such as Fig.

[32] N. F. Bali, G. F. Chew, and A. Pignotti, Phys. Rev. Letters **19**, 614 (1967); Phys. Rev. **163**, 1572 (1967); University of California Radiation Laboratory Report No. UCRL-17980, 1967 (unpublished).
[33] F. Zachariasen and G. Zweig, Phys. Rev. **160**, 1322 (1967); **160**, 1326 (1967).
[34] Chan Hong-Mo, K. Kajantie, and G. Ranft, Nuovo Cimento **49A**, 157 (1967).
[35] Chan Hong-Mo, K. Kajantie, G. Ranft, W. Beusch, and E. Flaminio, Nuovo Cimento **51A**, 696 (1967).
[36] W. W. M. Allison and L. Lyons, Nuovo Cimento **51B**, 404 (1967).
[37] G. M. Fraser and R. G. Roberts, Nuovo Cimento **47A**, 339 (1967); Phys. Rev. **159**, 1297 (1967).
[38] K. Kajantie, Nuovo Cimento **53A**, 424 (1968).
[39] R. G. Roberts, Nuovo Cimento **53A**, 557 (1968).
[40] A. Capella and G. Ranft, Nuovo Cimento **55A**, 507 (1968).
[41] R. Blankenbecler and R. L. Sugar, Phys. Rev. **168**, 1597 (1968).
[42] J. Finkelstein and K. Kajantie, CERN Report TH. No. 857, 1967 (unpublished).
[43] Chang Hong-Mo, J. Loskiewicz, and W. W. M. Allison, CERN Report TH. No. 866, 1968 (unpublished).
[44] A. Capella, Orsay Report TH/No. 235, 1968 (unpublished).

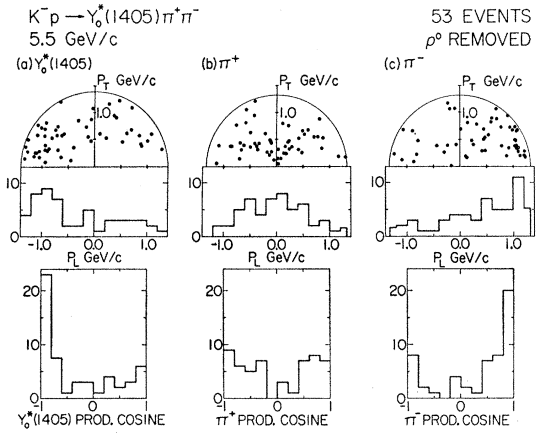

FIG. 12. Production features of $K^-p \to Y_0^*(1405)\pi^+\pi^-$. P_L and P_T are the longitudinal and transverse momenta in the overall c.m. system defined with respect to the incident K^- direction. (a) $Y_0^*(1405)$, (b) π^+, and (c) π^-.

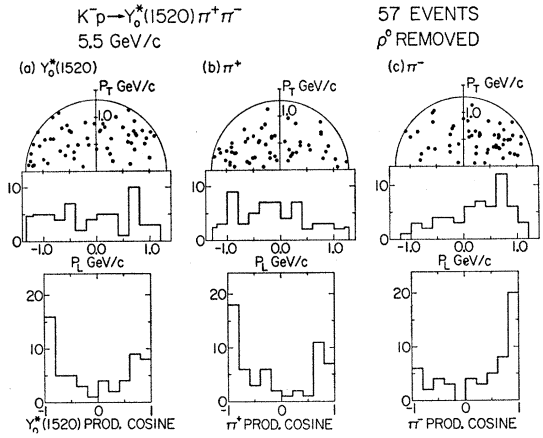

FIG. 14. Production features of $K^-p \to Y_0^*(1520)\pi^+\pi^-$. P_L and P_T are defined in the caption for Fig. 12. (a) $Y_0^*(1520)$, (b) π^+, and (c) π^-.

16(c), where e_1 and e_2 are strange, and e_1 cannot be pseudoscalar.

The production properties for $Y_0^*(1520)\pi^+\pi^-$ events (Fig. 14) are somewhat different from the preceding two channels. Although the π^- is generally produced in the forward direction, the $Y_0^*(1520)$ and the π^+ both exhibit rather isotropic production. This situation could perhaps be understood by a combination of diagrams in Figs. 16(a) and 16(b).

The production properties for the $\Sigma^-\pi^+\rho^0$ events are shown in Fig. 15. The features in this channel are suggestive of a mechanism such as the diagram in Fig. 16(d) for which baryon as well as meson exchange occurs. Also, the number of events in this channel relative to that of the $\Sigma^+\pi^-\rho^0$ channel (recall that only the $\Sigma^+ \to \pi^+ n$ decays are considered in Fig. 13) is indicative of a smaller cross section (see Table VI), as expected for baryon exchange relative to meson exchange.

E. Reactions $K^-p \to \Sigma^\pm\pi^\mp\pi^+\pi^-\pi^0$

In the investigation of this final state we restricted our attention to (a) events involving the $\omega^0(783)$ meson, and (b) the question of an enhancement in the $(\pi^\pm\pi^+\pi^-)$ spectra in the vicinity of 960 MeV/c^2 (the region of the δ meson). The ω^0 events appear in both the quasi-two-body ($Y^*\omega^0$) and quasi-three-body ($\Sigma^\pm\pi^\mp\omega^0$) configurations. Again, the Σ^+ events associated with the $\Sigma^+ \to p\pi^0$ decay were not considered.

1. General Features of the Reactions

Figure 17 shows a triangle plot of the invariant mass of $(\pi\pi\pi)^0$ versus that of $(\Sigma\pi)^0$, where both reactions have been added together and two combinations per event appear. The $\omega^0(783)$, $Y_0^*(1405)$, and $Y_0^*(1520)$ resonances may be distinguished as bands on the scatter plot and as peaks in the projections. The singly charged three-pion invariant-mass plots are shown in Fig. 18, and are discussed below.

2. Quasi-Two-Body Production: $Y_0^*\omega^0$

The mass resolution for the $(\pi\pi\pi)^0$ system in the vicinity of the ω^0 is of the order of 40 MeV/c^2, much

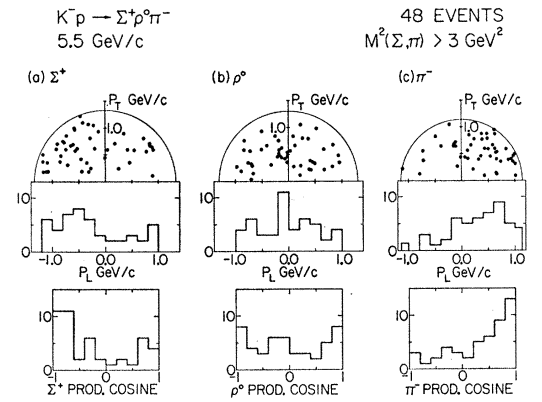

FIG. 13. Production features of $K^-p \to \Sigma^+\rho^0(770)\pi^-$. P_L and P_T are defined in the caption for Fig. 12. (a) Σ^+, (b) $\rho^0(770)$, and (c) π^-.

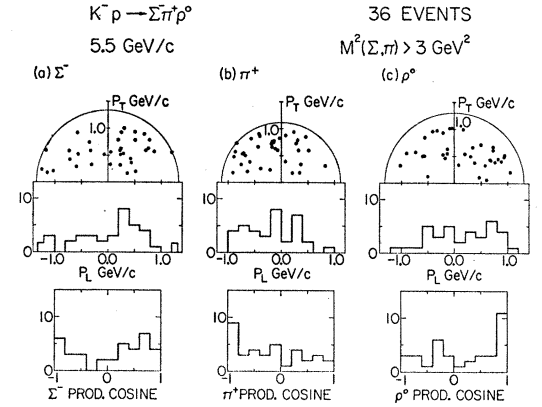

FIG. 15. Production features of $K^-p \to \Sigma^-\pi^+\rho^0(770)$. P_L and P_T are defined in the caption of Fig. 12. (a) Σ^-, (b) π^+, and (c) $\rho^0(770)$.

larger than the resonant width. Consequently, to select the ω^0 events, we used a rather wide mass slice

$$0.730 \leq M(\pi\pi\pi)^0 < 0.835 \text{ GeV}/c^2.$$

Figure 19 shows the invariant-mass distribution for the $(\Sigma\pi)^0$ system opposite the ω^0 events selected by means of the preceding mass slice. For a few events where both $(\pi\pi\pi)^0$ combinations satisfy this selection, both $(\Sigma\pi)^0$ combinations are plotted as shaded events. Quasi-two-body $Y^*\omega^0$ production is indicated by the presence of $Y_0^*(1405)$, $Y_0^*(1520)$, and $Y^*(\sim 1690)$ peaks. The c.m. production angular distributions for $Y_0^*(1405)\omega^0(783)$ and $Y_0^*(1520)\omega^0(783)$ events are given in Figs. 22(c) and 22(g). Cross sections for these channels are given in Table VI.

Production in the $Y_0^*(1520)\omega^0(783)$ channel has been observed previously at 3.8 GeV/c,[45] where both a peripheral peak and a flat component are seen in the c.m. production cosine distribution. Our data do not show a substantial flat component in this distribution.

3. *Quasi-Three-Body Production:* $\Sigma^+\pi^-\omega^0(783)$

In the same spirit as Sec. III D 7, we show in Fig. 20 the production properties of the $\Sigma^+\pi^-\omega^0(783)$ events, selected by the mass criteria

$$0.730 \leq M(\pi\pi\pi)^0 \leq 0.835 \text{ GeV}/c^2$$

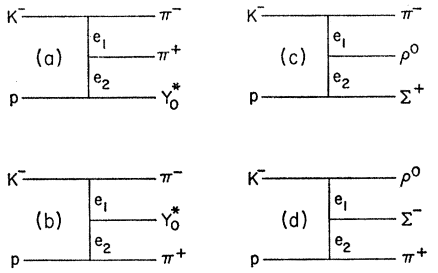

FIG. 16. Possible multiperipheral diagrams for the quasi-three-body final states. (a) $K^-p \to Y_0^*\pi^+\pi^-$, double meson exchange; (b) $K^-p \to Y_0^*\pi^+\pi^-$, meson plus baryon exchange; (c) $K^-p \to \Sigma^+\rho^0\pi^-$, double meson exchange; and (d) $K^-p \to \Sigma^-\pi^+\rho^0$, meson plus baryon exchange.

and

$$M(\Sigma\pi)^0 \geq 1.730 \text{ GeV}/c^2.$$

The Σ^+ is generally produced in the backward direction, the π^- in the forward direction, and the ω^0 at rest in the over-all c.m. system. A multiperipheral diagram such as Fig. 16(c), with ω^0 replacing ρ^0, might be invoked to explain these production features.

4. *Question of the* δ *(960) Meson*

Experimental evidence concerning the existence of a charged nonstrange meson with mass near 960 MeV/c^2, usually referred to as the δ meson, is presently confusing

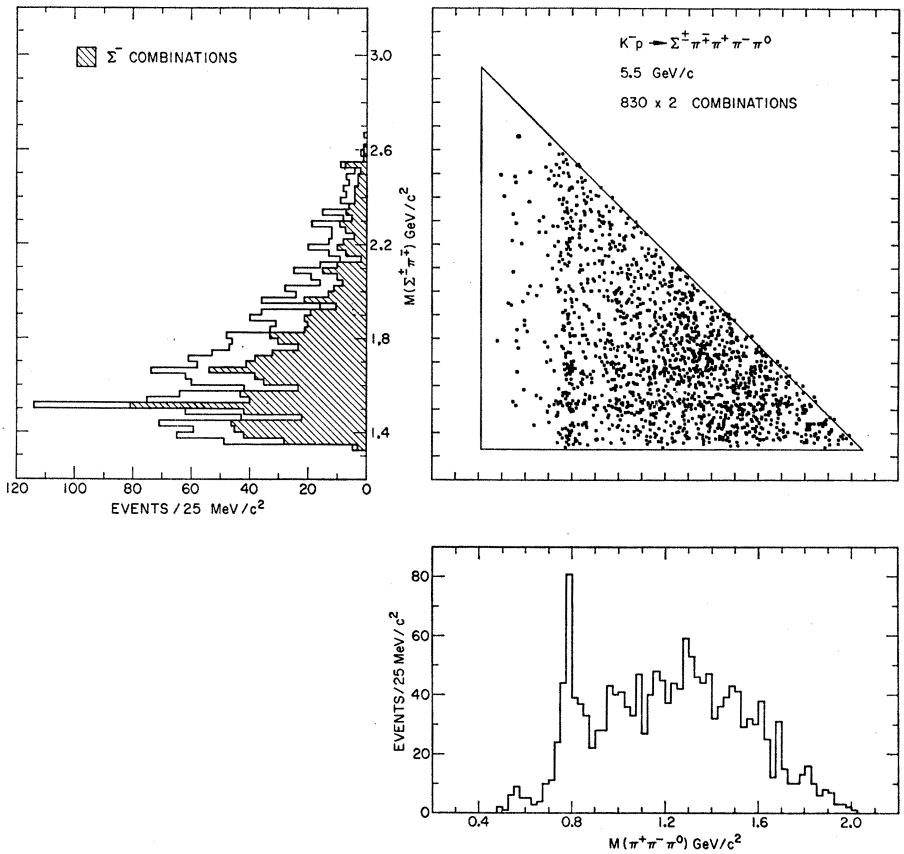

FIG. 17. Triangle plot and projections for both combinations of $(\Sigma\pi)^0$ versus $(\pi\pi\pi)^0$ from the reactions $K^-p \to \Sigma^{\pm}\pi^{\mp}\pi^+\pi^-\pi^0$.

[45] D. Duane Carmony, T. Hendricks, and Richard L. Lander, Phys. Rev. Letters 18, 615 (1967).

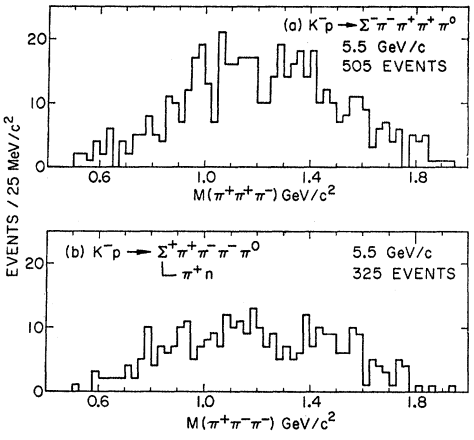

FIG. 18. Invariant-mass spectra for $(\pi^\pm\pi^+\pi^-)$ from the reactions $K^-p \to \Sigma^\mp\pi^0\pi^\pm\pi^+\pi^-$. (a) $M(\pi^+\pi^+\pi^-)$ seen in $K^-p \to \Sigma^-\pi^0\pi^+\pi^+\pi^-$; (b) $M(\pi^+\pi^-\pi^-)$ seen in $K^-p \to \Sigma^+\pi^0\pi^+\pi^-\pi^-$.

and somewhat contradictory.[9,46–52] Positive evidence for the δ^+ and δ^- has been reported at 6.0 GeV/c in the reactions $K^-p \to \Sigma^\pm\pi^0\delta^\mp$, $\delta^\mp \to (\pi^\mp\pi^+\pi^-)$.[9] In the 6.0-GeV/$c$ data, the δ^- was observed at 913 ± 25 MeV/c^2 with a width less than 30 MeV/c^2, while the δ^+ was observed at 939 ± 15 MeV/c^2 with a width less than 25 MeV/c^2.

It is of interest, therefore, to compare our results at 5.5 GeV/c to those at 6.0 GeV/c. The relevant mass spectra are shown in Fig. 18. Unfortunately, we are able neither to confirm nor to refute the existence of the $\delta^\pm$ enhancements. In our $(\pi^+\pi^+\pi^-)$ spectrum there is, optimistically, a two-standard-deviation bump above background centered at 975 ± 15 MeV/c^2 with a width of $\sim$50 MeV/c^2. Note, however, that the position of this bump is about two standard deviations higher than the bump in the 6.0-GeV/c data. In the $(\pi^+\pi^-\pi^-)$ spectrum we see a slight excess of events in the vicinity of 925 MeV/c^2. Although the position of this excess coincides with that seen at 6.0 GeV/c, it is not, by itself, statistically significant.

F. Reactions $K^-p \to \Sigma^\pm\pi^\mp K^+K^-$

These reactions were studied only for evidence of $Y^*\varphi^0(1020)$ production. Figure 21 shows the triangle scatter plot of $(\Sigma\pi)^0$ versus (K^+K^-), along with the mass projections. The $\varphi^0(1020)$, $Y_0^*(1405)$, and the $Y_0^*(1520)$ states are clearly evident. Double resonance

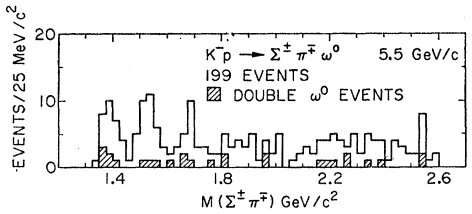

FIG. 19. Invariant-mass spectrum of $(\Sigma^\pm\pi^\mp)$ from the reactions $K^-p \to \Sigma^\pm\pi^\mp\omega^0(783)$. The ω^0 events are observed in the $(\pi^+\pi^-\pi^0)$ system and are required to lie in a mass interval 0.730–0.835 GeV/c^2. This rather wide interval has been used since the mass resolution in the ω^0 region is of the order of 40 MeV/c^2. Events for which both $(\pi^+\pi^-\pi^0)$ combinations fall in the ω^0 band are plotted twice, with both combinations shaded.

production in the $Y_0^*(1405)\varphi^0(1020)$ channel certainly is present, and a small $Y_0^*(1520)\varphi^0(1020)$ signal perhaps is present, also. In Fig. 22(d) and 22(h) the c.m. production angular distributions for these quasi-two-body channels are presented. The mass intervals used to select these events are as follows:

$$\varphi^0(1020): 1.010 \leq M(K^+K^-) \leq 1.030 \text{ GeV}/c^2,$$
$$Y_0^*(1405): 1.350 \leq M(\Sigma\pi)^0 \leq 1.460 \text{ GeV}/c^2,$$
$$Y_0^*(1520): 1.490 \leq M(\Sigma\pi)^0 \leq 1.550 \text{ GeV}/c^2.$$

Both productions are peripheral. The cross sections for these channels are given in Table VI.

IV. SUMMARY

Cross sections for the various channels involving resonant states are collected and presented in Table VI. Any reasonable production model would assume that all of these reactions involve strangeness or baryon exchange; hence the very small cross sections are not surprising. As a function of energy, strangeness, and baryon exchange, reactions are known to show a rapid rise in cross section immediately after the threshold, soon followed by a precipitous drop in cross section.[53]

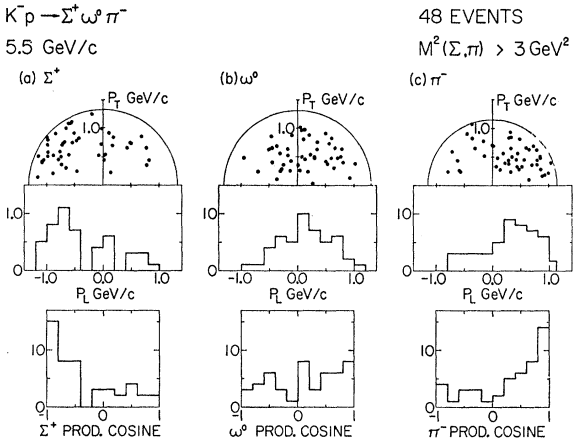

FIG. 20. Production features of $K^-p \to \Sigma^+\omega^0(783)\pi^-$. P_L and P_T are defined in the caption of Fig. 12. (a) Σ^+, (b) $\omega^0(783)$, and (c) π^-.

[46] W. Kienzle, B. C. Maglic, B. Levrat, F. Lefebvres, D Freystag, and H. R. Blieden, Phys. Letters **19**, 438 (1965).
[47] D. D. Allen, G. P. Fisher, G. Godden, L. Marshall, and R. Sears, Phys. Letters **22**, 543 (1966).
[48] J. Oostens, P. Chavanon, M. Crozon, and T. Tocqueville, Phys. Letters **22**, 708 (1966).
[49] M. Banner, M. L. Fayoux, J. L. Hamel, J. Zsemberg, J. Cheze, and J. Teiger, Phys. Letters **25B**, 300 (1967).
[50] M. Banner, J. Cheze, J. L. Hamel, G. Marel, J. Teiger, J. Zsemberg, P. Chavanon, M. Crozon, and L. K. Rangan, Phys. Letters **25B**, 569 (1967).
[51] Angela Barbaro-Galtieri, Maxine Matison, Alan Rittenberg, and Frank T. Shively, Phys. Rev. Letters **20**, 349 (1968).
[52] Saclay-Amsterdam-Bologna-Weizmann Institute-Paris Collaboration, Phys. Letters **26B**, 674 (1968).
[53] D. R. O. Morrison, Phys. Letters **22**, 528 (1966).

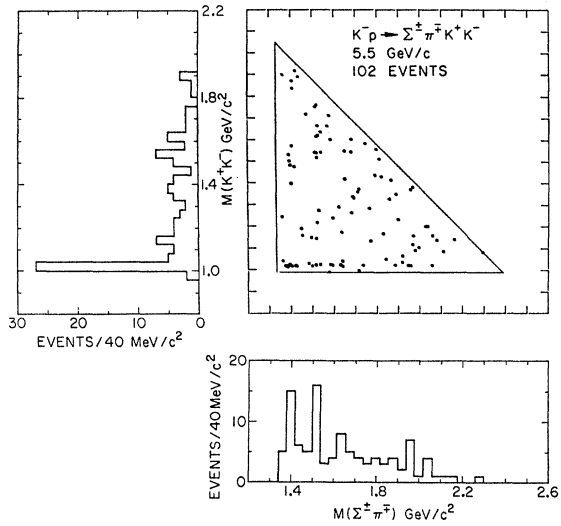

FIG. 21. Triangle plot and projections for $(\Sigma^{\pm}\pi^{\mp})$ versus (K^+K^-) from the reactions $K^-p \to \Sigma^{\pm}\pi^{\mp}K^+K^-$.

Although the experimental situation is certainly incomplete at present, such trends seem to hold for the reactions reported here when compared to experiments at other energies.

The c.m. production cosine distributions for the various quasi-two-body channels involving the $Y_0^*(1405)$ or $Y_0^*(1520)$ states are gathered in Fig. 22. Although the statistics are poor, and there may be background present in some channels, all show the characteristic peripheral peak associated with meson exchange.[54] The $Y_0^*(1520)$ reactions have a few events in the antiperipheral regions, suggestive of baryon-exchange contributions.

For the $K^-p \to \Sigma^+\rho^-$ reaction, we have investigated the differential cross section and density matrix elements in the peripheral region. The density matrix elements clearly imply a dominance of natural-parity exchange. The experimental value of the forward differential cross section relative to that of the $K^-p \to \Sigma^+\pi^-$ reaction has been found to disagree with a prediction made by Arnold.

We have studied the production features of the quasi-three-body reactions

$$K^-p \to Y_0^*(1405)\pi^+\pi^-,$$
$$K^-p \to Y_0^*(1520)\pi^+\pi^-,$$
$$K^-p \to \Sigma^{\pm}\pi^{\mp}\rho^0(770),$$
$$K^-p \to \Sigma^+\pi^-\omega^0(783).$$

The results suggest the presence of multiperipheral mechanisms.

We have searched for evidence for the $\delta^{\pm}(960)$ meson in the reactions $K^-p \to \Sigma^{\pm}\pi^0\delta^{\mp}$ and $\delta^{\mp} \to (\pi^{\mp}\pi^+\pi^-)$, with inconclusive results. A small excess of events, not statistically significant, was observed in the $(\pi^+\pi^-\pi^-)$ spectrum coincident with the bump reported at 6.0 GeV/c; a two-standard-deviation bump was observed in the $(\pi^+\pi^+\pi^-)$ spectrum, but centered $\sim$40 MeV/c^2 higher than that reported at 6.0 GeV/c.

[54] J. D. Jackson, Rev. Mod. Phys. **37**, 484 (1965); in *Proceedings of the Thirteenth International Conference on High Energy Physics, Berkeley, 1966* (University of California Press, Berkeley, 1967), p. 149.

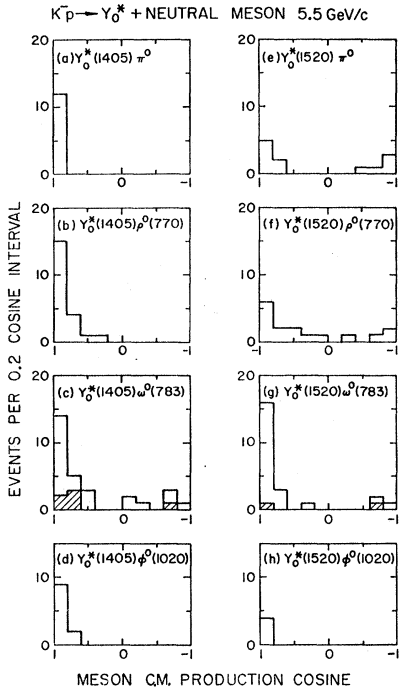

FIG. 22. Center-of-mass production cosine distributions for various reactions of the type $K^-p \to Y_0^*$+neutral meson. The final states used in these distributions are indicated below: (a) $Y_0^*(1405)\pi^0$, $Y_0^* \to \Sigma^-\pi^+$; (b) $Y_0^*(1405)\rho^0(770)$, $Y_0^* \to \Sigma^{\pm}\pi^{\mp}$, $\rho^0 \to \pi^+\pi^-$; (c) $Y_0^*(1405)\omega^0(783)$, $Y_0^* \to \Sigma^{\pm}\pi^{\mp}$, $\omega^0 \to \pi^+\pi^-\pi^0$; (d) $Y_0^*(1405)\varphi^0(1020)$, $Y_0^* \to \Sigma^{\pm}\pi^{\mp}$, $\varphi^0 \to K^+K^-$; (e) $Y_0^*(1520)\pi^0$, $Y_0^* \to \Sigma^-\pi^+$; (f) $Y_0^*(1520)\rho^0(770)$, $Y_0^* \to \Sigma^{\pm}\pi^{\mp}$, $\rho^0 \to \pi^+\pi^-$; (g) $Y_0^*(1520)\omega^0(783)$, $Y_0^* \to \Sigma^{\pm}\pi^{\mp}$, $\omega^0 \to \pi^+\pi^-\pi^0$; and (h) $Y_0^*(1520)$-$\varphi^0(1020)$, $Y_0^* \to \Sigma^{\pm}\pi^{\mp}$, $\varphi^0 \to K^+K^-$. For (a) and (e), the $Y_0^* \to \Sigma^+\pi^-$ decay is not included because the final state $\Sigma^+\pi^-\pi^0$ is complicated by $\Sigma^+\rho^-(770)$ production. In all other distributions, only $\Sigma^{\pm} \to \pi^{\pm}n$ decays are included. In (c) and (g), the "double ω^0" events are shaded. No background subtractions have been attempted in these distributions. The resonances were defined by the following mass intervals:

$$Y_0^*(1405): 1.350 \leq M(\Sigma\pi) \leq 1.460 \text{ GeV}/c^2;$$
$$Y_0^*(1520): 1.490 \leq M(\Sigma\pi) \leq 1.550 \text{ GeV}/c^2;$$
$$\rho^0(770): 0.670 \leq M(\pi^+\pi^-) \leq 0.870 \text{ GeV}/c^2;$$
$$\omega^0(783): 0.730 \leq M(\pi^+\pi^-\pi^0) \leq 0.835 \text{ GeV}/c^2;$$

and

$$\varphi^0(1020): 1.010 \leq M(K^+K^-) \leq 1.030 \text{ GeV}/c^2.$$

ACKNOWLEDGMENTS

We are grateful for the assistance given to us by the ZGS and bubble-chamber staffs at Argonne. Without the cooperation of the bubble-chamber groups at Argonne, Northwestern University, and the University of Wisconsin this exposure would not have been possible. We also wish to acknowledge the capable work of many individuals, too numerous to mention, on the scanning and measuring crews, the supervisory staff, the engineering staff, and the programming staff at the University of Illinois.